coatings

Article

Numerical Study on Particle Behavior and Deposition Accuracy in Cold Spray Additive Manufacturing

Saeed Garmeh [1] and Mehdi Jadidi [2,*]

[1] Department of Mechanical, Industrial and Aerospace Engineering, Concordia University, Montreal, QC H3G 1M8, Canada
[2] Department of Mechanical and Industrial Engineering, University of Toronto, Toronto, ON M5S 3G8, Canada
* Correspondence: mehdi.jadidi@utoronto.ca

Abstract: Cold Spray additive manufacturing (CSAM) is an emerging technique to fabricate free-standing objects by depositing solid-state layers of materials. Thanks to its remarkable deposition rate and maneuverability, it can be tailored to manufacturing intricate geometries in aerospace industries. In comparison to other additive manufacturing techniques, it is the processing speed, solid-state deposition, and the cost that make CSAM unique. In this study, CSAM process was modeled for a system comprised of a high-pressure cold spray gun with axial powder injection. To represent the flow structure around the already built objects and the deposited layers of CSAM, three walls with different profiles are placed on a flat substrate. In this work, the gas-particle behaviors are studied at the vicinity of these non-axisymmetric objects that can be generalized to more complex geometries and the applications of CSAM. The model is 3D and aluminum and copper powders were used for the feedstock. The particles' conditions upon impact, such as particles' footprint and normal impact velocities are studied. The numerical results show that the deviation of particles which is caused by the supersonic flow inside the nozzle and the shock waves outside the nozzle defines the accuracy of the deposition. Furthermore, the results manifest the particle's material and size have a significant influence on the acquired velocities and trajectories of the particles, and consequently on the resolution of the process. It is found that the profile of the deposited layers has some effects on the gas flow near the substrate which plays a role in the dispersion of fine particles.

Keywords: additive manufacturing; cold spray; numerical simulation

Citation: Garmeh, S.; Jadidi, M. Numerical Study on Particle Behavior and Deposition Accuracy in Cold Spray Additive Manufacturing. *Coatings* **2022**, *12*, 1546. https://doi.org/10.3390/coatings12101546

Academic Editor: Sergey N. Grigoriev

Received: 31 August 2022
Accepted: 12 October 2022
Published: 14 October 2022

1. Introduction

Cold spray (CS) is a non-thermal deposition process using particles in solid-state to build a coating layer. CS has been used to form protective thick coatings as well as free form 3D shapes [1]. Commonly, this technique is applied for the deposition of metal powders such as copper and aluminum, as well as nickel alloys, stainless steel, Inconel superalloys, etc. [2–5]. This spraying process also allows deposition onto erodible materials such as polymers, composites and ceramics [6,7]. In CS, particles are accelerated by a supersonic flow of nitrogen, helium, or air up to 500–1000 m/s while their temperature remains below the melting point. The supersonic gas flow is generated by flowing pressurized gas into a converging-diverging nozzle which is embedded in the CS gun [8,9]. At such a high speed, particles have notable kinetic energy which results in localized plastic deformation of both particles and substrate upon impact. The bonding occurs through mechanical interlocking and adiabatic shear instability [10,11]. The particle size ranges from 1 to 50 μm, however, particles with diameters smaller than 10 μm are not desirable since they do not contribute much to the coating and they cause nozzle clogging [12–15].

CS can be used to form free-standing shapes, which is called cold spray additive manufacturing (CSAM). Thanks to its high throughput, it can produce complex shapes with build rates much higher than other additive manufacturing technologies [15]. In

CSAM, a 3D object is produced by the deposition of layers on top of each other. This layer-by-layer approach permits the formation of complex parts that cannot be fabricated with conventional machining. Today, CSAM is known as one of the most developed AM techniques while dealing with oxygen and temperature-sensitive materials [2,16]. Although CSAM has unique advantages, there are some drawbacks associated with this technique. The main downside is the relatively low resolution of the process (i.e., the low accuracy of the deposition). If the resolution is not high enough, it may be required to machine the parts after manufacturing with CSAM. However, it is shown that the accuracy can be enhanced to some extent by using micro nozzles [8,17].

Several articles about predicting and controlling the cold spray deposit profile have been recently published. Wu et al. [18] formulated a special spray strategy to control the shape of deposits during CSAM. In their work, three parameters were controlled: the angle between the nozzle and the substrate, the offset distance between the deposit and the nozzle centerline, and the distance between the nozzle exit and the substrate. In another work [19], they used a 3D profiler to assess the morphology of deposited coatings online and the data was transferred to a robot controller to optimize the kinematic parameters in real time. Ikeuchi et al. [20] developed a data-efficient neural network for track profile modeling in CSAM and to predict additively manufactured geometry. Vanerio et al. [21] developed a 3D model which is able to simulate the cold spray deposit profile. In their model, the effects of different parameters, like the number of scanning passes, spray angle, curved substrates, shadow effect and non-Gaussian profiles, scanning speed and stand-off distance were considered. Moreover, computational fluid dynamics (CFD) has been used to understand and optimize the cold spray process. For instance, Özdemir et al. [22] used particle velocimetry together with numerical simulations to understand the key physical factors that affect the particle velocity and coatings buildup. It was found that, particle sphericity is one of the main parameters that affect the particle velocity. In addition, the effects of turbulence models on the predictions of particle trajectory and velocity were discussed. In another study, Özdemir et al. [23] modeled the heat generation due to gas impingement and particle plastic deformation in the cold spray process. Sudhan et al. [24] also used CFD simulations to design a new cold spray nozzle. A bell-type geometry was assumed for divergent section of the nozzle in their study. In addition, transverse and axial powder injections were analyzed. The compactness of the system and the axial alignment of the spray were the main benefits of using a bell-type nozzle. In addition, it was shown that particle impact velocity is higher for axial injection compared to that for transverse injection under similar operating conditions.

In the present study, to understand the key reasons affecting the resolution of a typical CSAM process, the influence of supersonic flow, shock diamonds, particle size and type, and geometry of the manufactured part on the particle in-flight behavior are investigated. There are stagnation points where the pressure builds up and forms a bow shock. The bow shock has a direct effect on the particles' trajectories as well as their normal impact velocity. Furthermore, deposition on the layers already built could be challenging since there might be inclined surfaces and sharp edges that change the direction of the flow of gas and particles. As a result, it could reduce the accuracy and efficiency of the deposition.

In this study, a high-pressure cold spray system with axial powder injection is simulated. Two different walls with uniform and non-uniform cross-sections are placed on top of a flat substrate to mimic the complex geometries like the already built walls (in industry, there are geometries like a hole, a step, layers already built, a wall, etc.). In this case, the possibility of building layers on top of a vertical and inclined wall can be investigated. Moreover, the profile of the deposited layer in Kotoban et al.'s work [25] is modeled and placed on the substrate. It is worth mentioning that the walls are non-axisymmetric and 3D which can be good examples of complex geometries observed in CSAM. The main novelty of the present study is to understand the flow structure around these complex objects. To examine the effect of particle material, aluminum and copper powders are injected. A Rosin-Rammler particle size distribution based on the experimental study of Samareh et al. [26] is used to model the particles in-flight and upon impact conditions. Numerical modeling presented in this work can also shed light on the shape of deposited layers and the final cut of the objects in CSAM.

2. Methodology

2.1. Geometry

In this work, a high-pressure commercial cold spray equipment KINETIKS 3000 is studied. The schematic of the nozzle and substrates with the mentioned walls/objects are presented in Figure 1. The converging-diverging nozzle is attached to the stagnation chamber where the high-pressure gas enters. Diameters of the nozzle inlet, throat, and exit are 14, 3.2, and 6.6 mm, respectively. The gun is equipped with an axial powder injection having a diameter of 3 mm that injects particles 50 mm upstream the nozzle throat.

2.2. Computational Domain

The computational domain is shown in Figure 2. The domain is extended 100 mm axially and 30 mm radially from the nozzle exit. The studied grid consists of 1,460,816 quadrilateral cells. The grid is generated using ICEM CFD v18.2. A grid independence study was carried out to certify the results are independent of the mesh size. A flat substrate is placed at the stand-off distance (SOD) of 30 mm from the nozzle exit. On top of that, three objects are placed, each with a height of 5 mm, resulting in a SOD of 25 mm from the nozzle exit. There is a vertical wall (uniform cross-section), an inclined wall (non-uniform cross-section), and a smooth wall based on the experimental study of Kotoban et al. [25] that are presented in Figures 1 and 2. It should be pointed out that the vertical and inclined walls are imaginary and are considered to study the particle inflight behavior near complicated geometries. The deposited wall in Kotoban et al.'s work and the smooth wall modeled in the current study are shown in Figure 3 side-by-side.

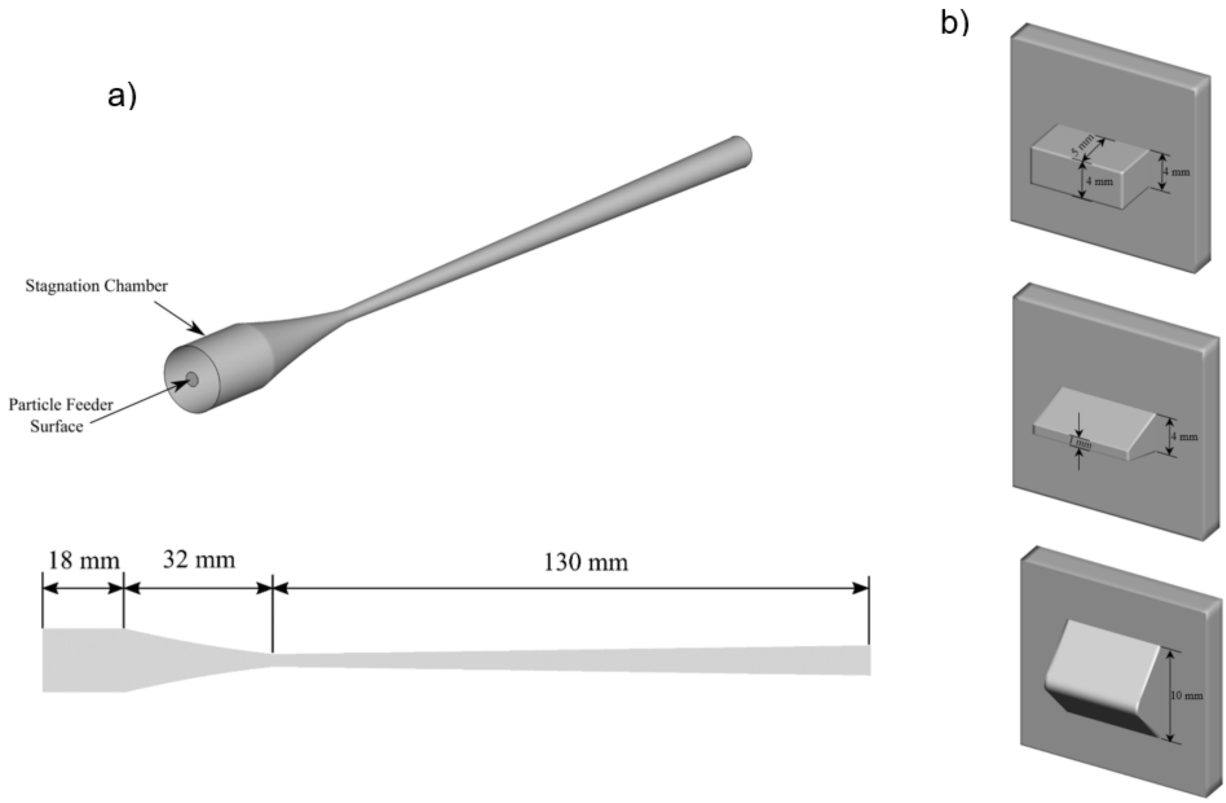

Figure 1. (**a**) Nozzle schematic and (**b**) the objects on top of the flat substrate.

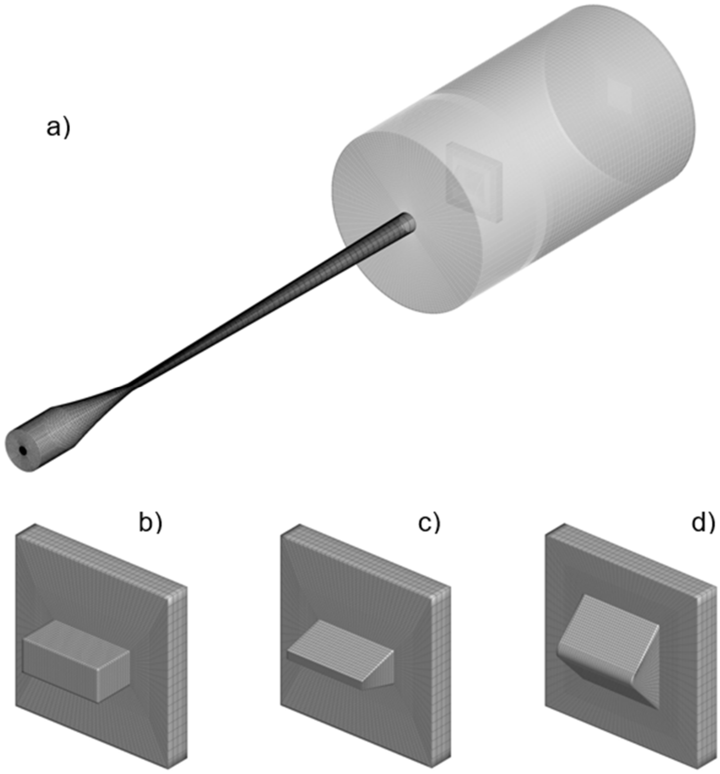

Figure 2. (**a**) Computational domain, (**b**) Mesh for vertical wall with a uniform cross-section, (**c**) Mesh for Inclined wall with non-uniform cross-section, and (**d**) Mesh for smooth wall.

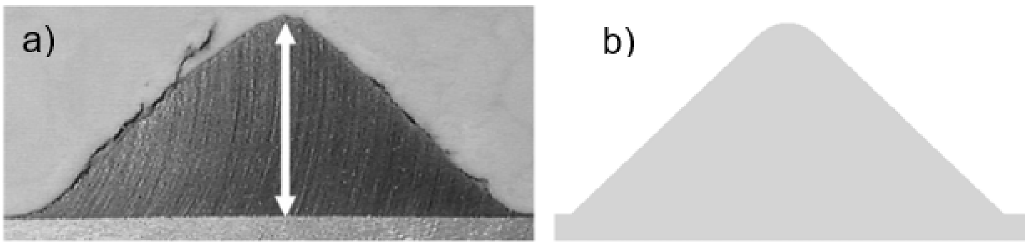

Figure 3. Deposition profile in (**a**) Kotoban et al.'s work (Adapted from Reference [25] with permission (Copyright Elsevier 2017)) and (**b**) the current study.

2.3. Boundary Conditions

Following the experimental study of Samareh et al. [26], the boundary conditions are applied accordingly. For the inlet boundary condition, the pressure inlet was used. According to [26], inlet pressure is set to 2.9 MPa (gauge) and the gas temperature is 614 K. The injector pressure is set to 2.94 MPa. Particles are injected from the feeder surface shown in Figure 1. Copper and aluminum particles with the feed rate of 1 g/s are injected from the feeder. For each powder type, the same Rosin-Rammler size distribution was used [26]. The Rosin-Rammler distribution is presented in Figure 4. The carrier gas is nitrogen, and it discharges to the atmospheric pressure. Therefore, the pressure outlet is set as the outlet boundary condition and it is applied far from the nozzle exit to avoid any unrealistic changes [27]. The nozzle, the substrate, and the objects on top of the flat substrate are set as walls with no-slip boundary conditions. They are set as adiabatic walls due to the negligible heat transfer [16]. The trap boundary condition is assigned to the substrate and the objects to capture the particles.

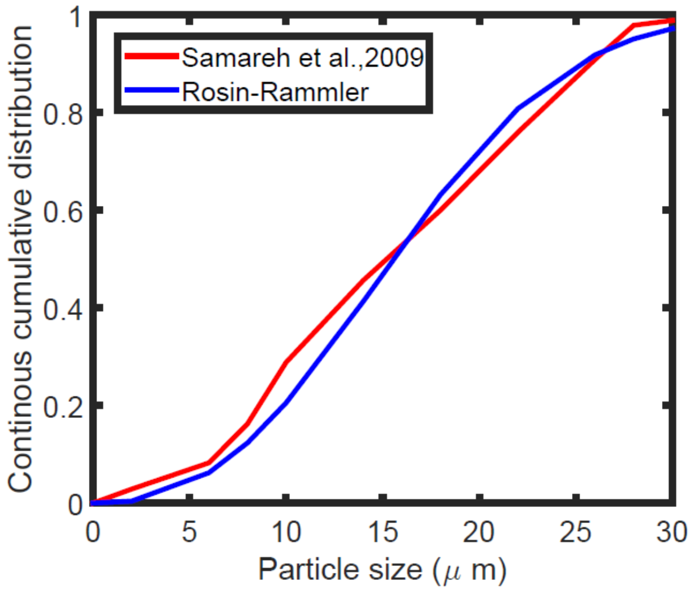

Figure 4. Particle size distribution [26].

2.4. Numerical Solver

ANSYS FLUENT v18.2 is used for numerical modeling. A steady-state solution with a pressure-based solver is used for solving the carrier gas. In addition to the compressible form of the mass, momentum, and energy conservation equations, the ideal gas law is applied to calculate the density and to take into account the compressibility effects. The compressibility factor for nitrogen has less than 4% deviation from the ideal gas law for pressures and temperatures up to 10 MPa and 900 K, respectively [26]. Therefore, it allows us to use the ideal gas assumption. The model is 3D, and the second-order scheme is used for solving all the governing equations. The realizable k-ε is used for turbulence modeling since it accurately estimates the spreading rate of planar and round jets and provides good performance for flows including rotation, separation, and recirculation [28–30]. A two-way coupled Eulerian-Lagrangian approach provided by the discrete phase model (DPM) is used for tracking the particles [29–31]. In other words, the effects of particles on the gas flow are taken into account using different source terms in mass, momentum and energy equations of the gas phase. In addition, in FLUENT, the work done by the turbulent eddies on the particles is subtracted from the turbulent kinetic energy based on the models developed in [32,33]. The drag force is modeled using the coefficient proposed by Crowe [34]. The mentioned drag coefficient is a function of Reynolds, Mach, and Knudsen numbers and considers the effects of compressibility and rarefaction on the particle dynamics. The thermophoretic force is enabled because of the temperature gradient in the gas flow, particularly near the substrate [28,35,36]. Pressure gradient and Saffman lift forces are used as the additional forces [28]. Particle dispersion due to the turbulence effects is also considered by a stochastic tracking type model [28,37]. It should be noted that the numerical modeling in the present study is mostly based on the works of Lupoi and O'Neill [37] and Samareh et al. [26]. In the work of Lupoi and O'Neill [37], the Stochastic-Tracking type model implemented in FLUENT was also used. In this method, the Discrete Random Walk (DRW) model is utilized to estimate the effect of turbulent velocity fluctuations on the particle trajectories. In the DRW model, the inputs are turbulent kinetic energy (k) and the rate of dissipation of turbulent kinetic energy (ε), and the fluctuating velocity components are discrete piecewise constant functions of time. When the path is calculated for a sufficient number of times, a reasonable estimation of the random effects by turbulence on particle dynamics can be obtained.

3. Results

3.1. Gas Phase

Firstly, the flat substrate case without the objects is simulated. It helps us to validate our model with the study of Samareh et al. [26]. By applying all the corresponding boundary conditions (inlet pressure = 29 bar, inlet temperature = 614 K), the simulation results are compared with the experimental data. For validation, we look into the oblique shock angle at the nozzle exit and the location of the shock diamonds. Figure 5 shows the pressure contours obtained from our numerical modeling and the shock visualization of the experiments performed by Siemens corporate technology in Berlin [26]. As shown by vertical dashed lines, the locations of the shocks are well predicted by the model. The angle of the oblique shock at the nozzle exit for the simulation is determined to be $\alpha = 25°$ and for the experiment $\beta = 23°$.

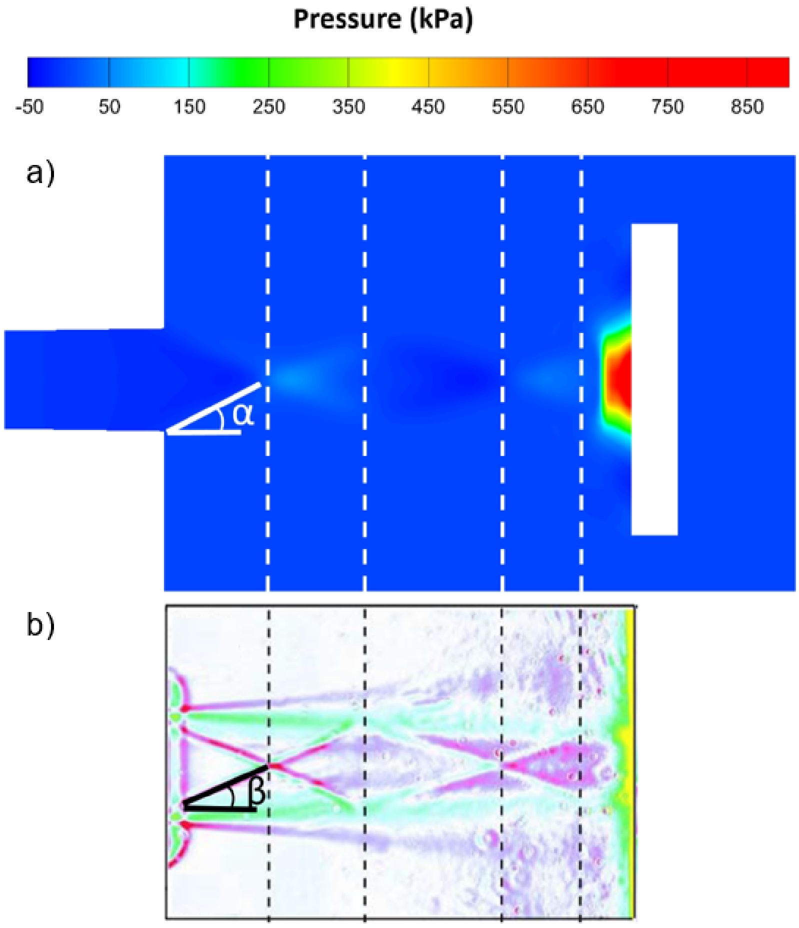

Figure 5. (**a**) Contours of pressure and (**b**) the visualization of shocks for the experiment presented in Samareh et al.'s work (Reproduced from Reference [26] with permission (Copyright Springer 2009)).

Placing objects on the flat substrate can considerably change the gas flow pattern. Pressure contours for the three shapes are presented in Figure 6. While exiting, the flow is over-expanded which results in the formation of an oblique shock at the nozzle exit. The minimum gauge pressure is found to be around −50 kPa before the oblique shock that increases up to 200 kPa after passing the oblique shock. Upon reaching the placed geometries, the flow experiences a sudden jump in the pressure. This jump is caused by the strong bow shock formed on all the three cases. However, the strength and location of the bow shock depend on the geometry of the objects. To better represent the shock diamonds and the flow structure near the substrate, iso-surfaces of the pressure at the nozzle exit are also illustrated in Figure 6b. The light blue color is the representative of the gauge pressure of −5 kPa, yellow is +5 kPa, and red is +8 kPa. The jumps of pressure between positive and negative values are attributable to the shock waves and expansion fans. Before the shock diamonds, the gauge pressure is negative. The pressure jump caused by the shock elevates the pressure to positive values and reduces the flow velocity. On the contrary, expansion fans reduce the pressure and increase the velocity. Usually, these two follow each other and the results are the oscillation of pressure at the nozzle exit and near the substrate.

Figure 7 shows the pressure distribution on the surface of the objects. For vertical (i.e., uniform cross-section) and inclined walls, the highest pressure buildup is around 1.2 MPa. The high-pressure area on top of the vertical wall is broader than the inclined wall and it can be expected that the bow shock formed on top of the vertical wall deflects the particles further. For the smooth wall, however, the surface pressure reaches around 1 MPa on the top, which can have a slightly weaker effect on particle deviation.

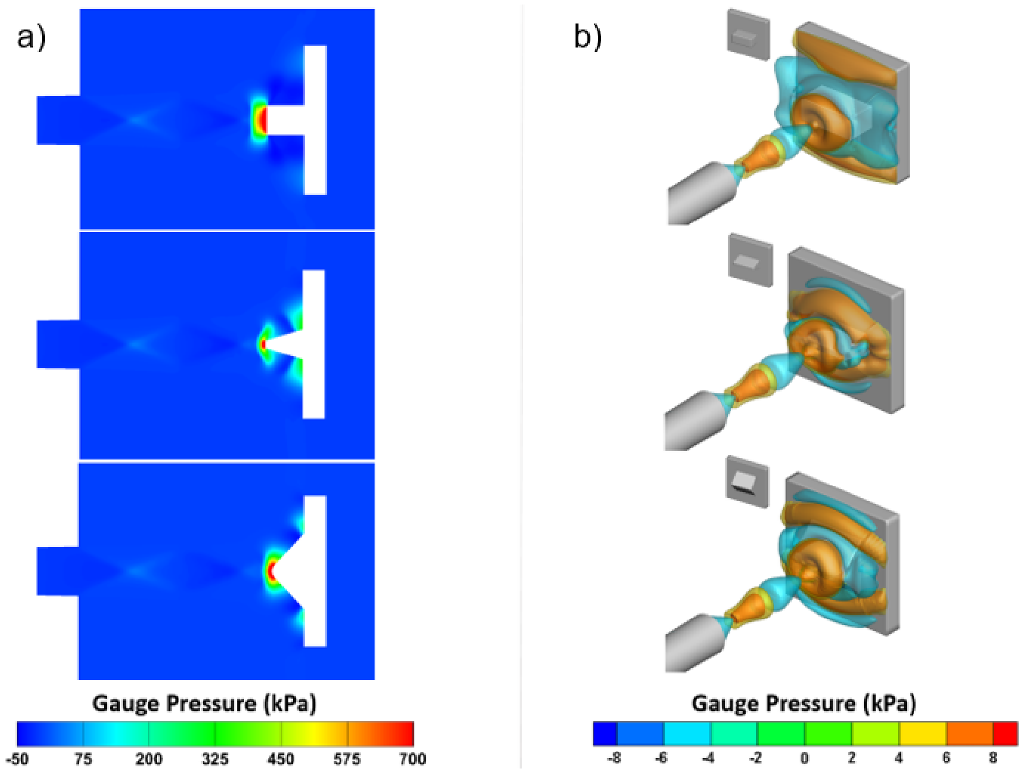

Figure 6. (**a**) Pressure contours and (**b**) iso-surfaces of pressure at the nozzle exit for the vertical wall (**top**), inclined wall (**middle**), and the smooth wall (**bottom**).

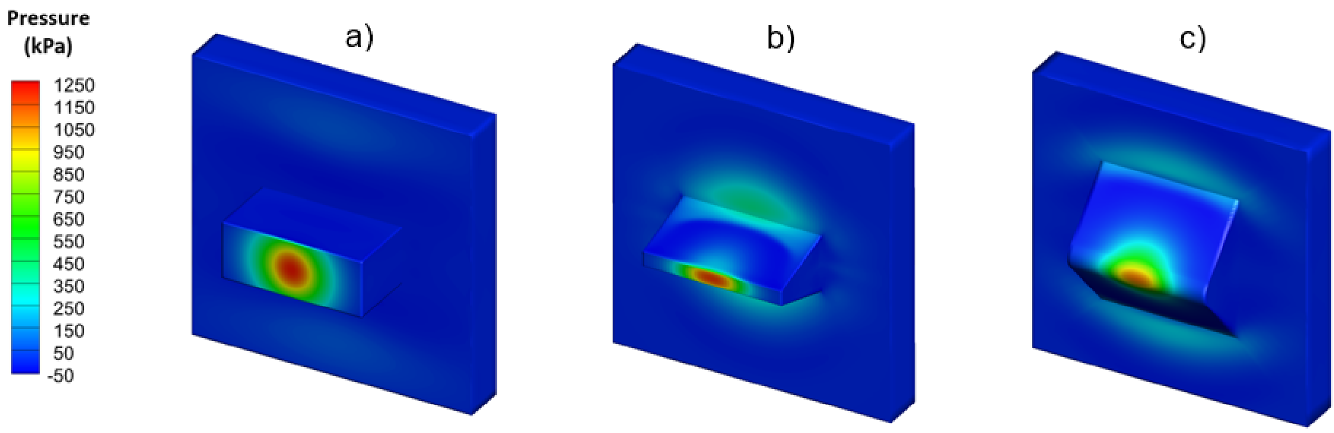

Figure 7. Pressure distribution on the surface of the (**a**) vertical, (**b**) inclined, and (**c**) the smooth walls.

Contours of Mach numbers for all the three cases are presented in Figure 8. The Mach number can define the flow regime, and it has a considerable influence on the particle drag coefficient [38]. The Mach number reaches 3 at the nozzle exit for all the cases. There is a subtle reduction in Mach number after passing through the shock waves. The velocity and consequently, the Mach number should reach zero on the surface of the walls due to the no-slip boundary condition. Hence, the flow experiences a sharp reduction in the velocity and Mach number near the walls. For the case with a vertical wall (i.e., uniform cross-section), this change is more abruptly than the other two cases and it indicates there is a stronger bow shock formed on top of this wall. For the inclined wall, the slope of the wall assists the flow to change its direction from axial to radial, however, at the base, there is a region with a low Mach number which points out a high-pressure region. For the smooth wall, considering the top curvature and its mild slope, the flow changes its direction more fluently and in general the Mach number remains greater at the top and the base in comparison to the other cases.

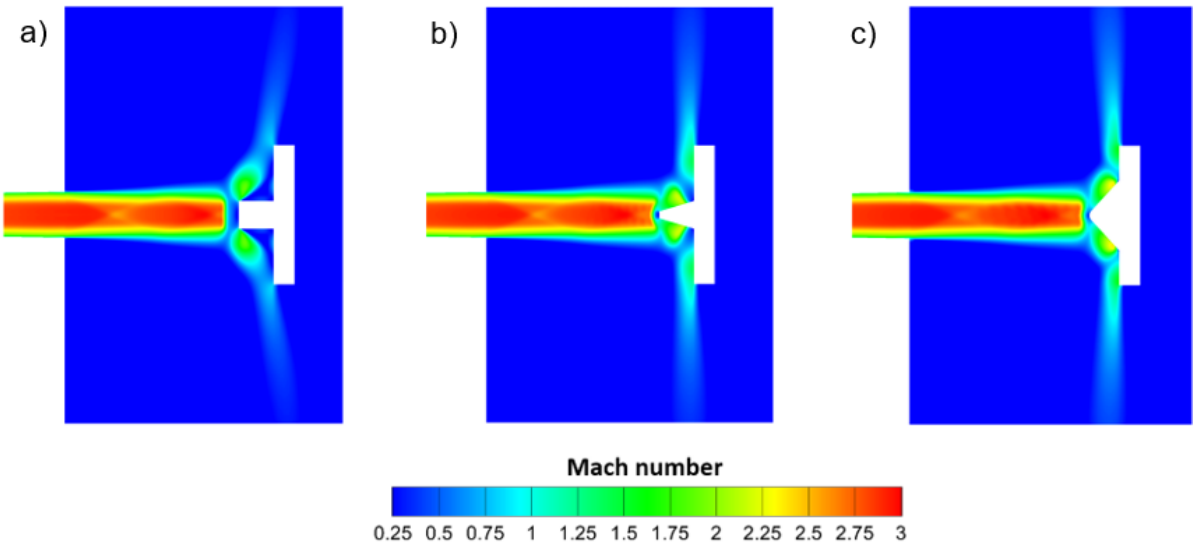

Figure 8. Mach number contour for the cases with (**a**) vertical wall, (**b**) inclined wall, and (**c**) the smooth wall.

3.2. Discrete Phase

By introducing the particles with the size distribution presented in Figure 4, the particles' conditions upon impact can be analyzed. Figure 9. Shows the particle footprints and their velocities at the Stand-off distance of 25 mm from the nozzle exit, right before impinging the top surface of the walls. It is worth mentioning that the aluminum density is almost a third of the copper density. As a result, the aluminum particles have slightly higher velocities, and they disperse on a broader area. The highest dispersion occurs for the aluminum particles impacting on the vertical wall. As presented in Figure 6, the vertical wall has the strongest bow shock, and it clearly deflects the small aluminum particles. Figure 9 also indicates that the distribution of particles for the inclined wall has an oval shape since the flow is redirecting along its inclined surfaces and carries them in that direction. The distribution of copper particles in the case with the smooth wall is slightly more packed than the other cases. Two factors of the higher density of copper particles and weaker bow shock contribute to having the highest resolution in this case.

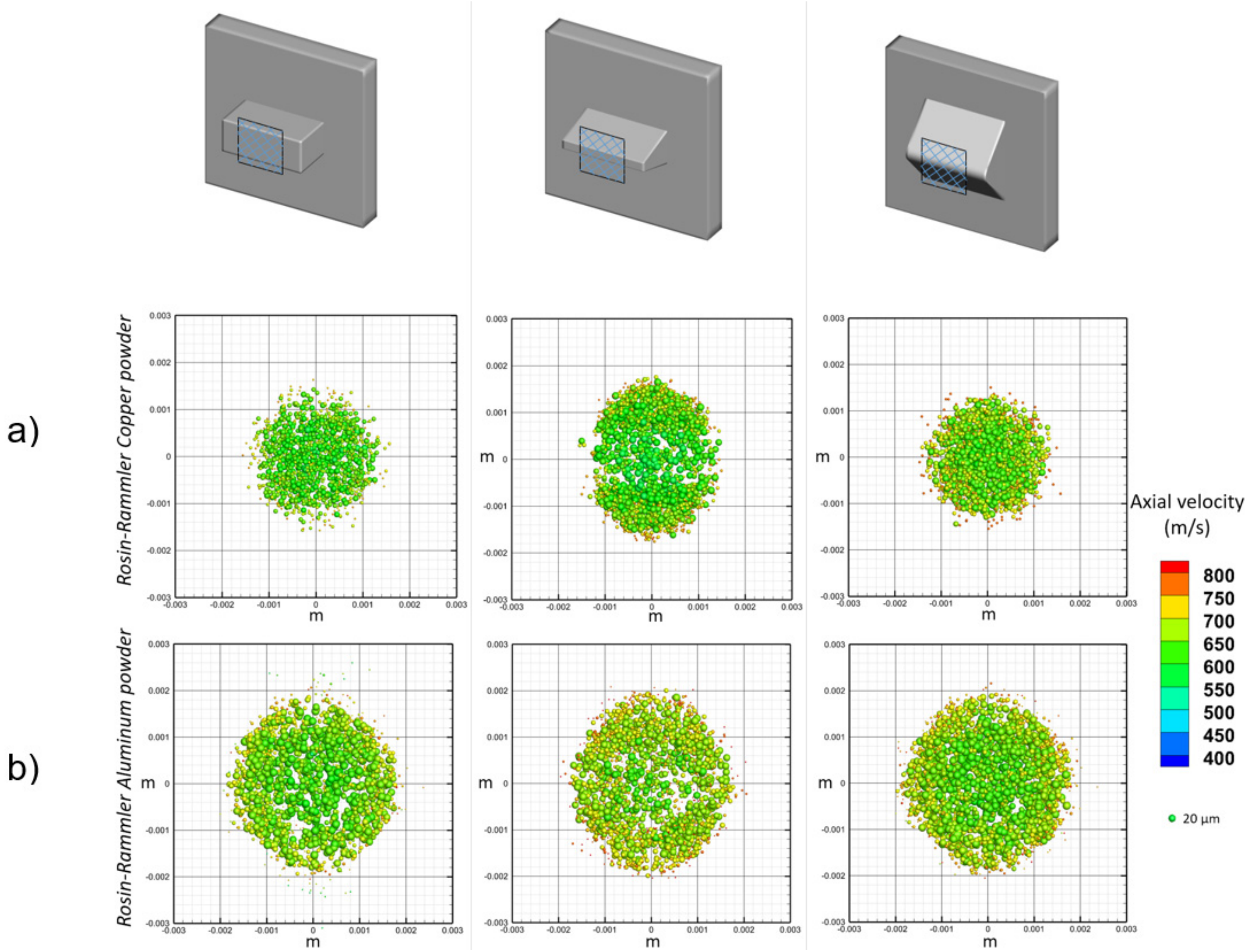

Figure 9. Distribution of (**a**) copper particles and (**b**) aluminum particles at SOD = 25 mm for the vertical wall (**left**), inclined wall (**middle**), and the smooth wall (**right**).

Bonding in CS is dependent on the normal impact velocity of the particle [13,39,40]. If it exceeds a certain material-dependent value, the so-called critical velocity, particle adheres to the substrate. The critical velocity for bonding depends particularly on the properties of the substrate and particle material as well as the particle diameter. Figures 10–12 show the particle normal impact velocities versus the radial location of particles. The radial location is defined as the distance of a particle from the nozzle centerline. Particle conditions for the case with the vertical wall are depicted in Figure 10. As can be seen, 10 and 20 µm aluminum particles acquire higher impact velocities in comparison to the copper particles due to their lower densities. However, the lower density of aluminum causes the small particles to decelerate faster while passing through the bow shock. This leads to a wider range of velocities and more dispersion of the 5 µm particles. Figure 11 represents the particles' impact condition for the case with the inclined wall. Similar to Figure 10, aluminum particles achieve higher velocities. For both cases, some particles impinge on the top surface of the wall. Normal impact velocities for these particles are significant. It is expected that they all adhere to the top surface of the wall. Differently, several particles impinge on the inclined sides of the wall which results in low normal impact velocities. The chance for these particles to coat the surface is low because their normal velocities are below the critical bonding speed. In Figure 11, those particles with normal impact velocities less than 300 m/s are indeed those impinging the sides of the inclined wall. To explain why for radii higher than 0.5 mm, both high and low particle velocities exist, the left image in

Figure 11 is demonstrated. As shown, the flow is not axisymmetric. When r < 0.5 mm, all the particles impact on the top surface. However, when r > 0.5 mm, some particles impact on the top and some particles impact on the side inclined planes. Therefore, two regions with high and low velocities are obtained.

Figure 12 shows the particles' conditions upon impact for the case with the smooth wall. In this case, the top surface is a curve, and it results in different surface normal vectors at each point and consequently, different normal impact velocities. As shown, by increasing the radial position, the normal velocity of many particles as well as the chance of particle deposition drop. According to our assumption for critical bonding velocities, for both aluminum and copper particles, some particles acquire the critical velocity. On the contrary, some particles do not achieve the critical velocity and they may form weak bonding or simply bounce off the substrate. Therefore, due to circular shape of nozzle cross-section, and since by increasing the radial distance from the nozzle centerline, both the concentration of the particles as well as the number density of high-speed particle decrease, a triangular deposit profile would be formed which has been observed in several studies [18–21,25,41–43].

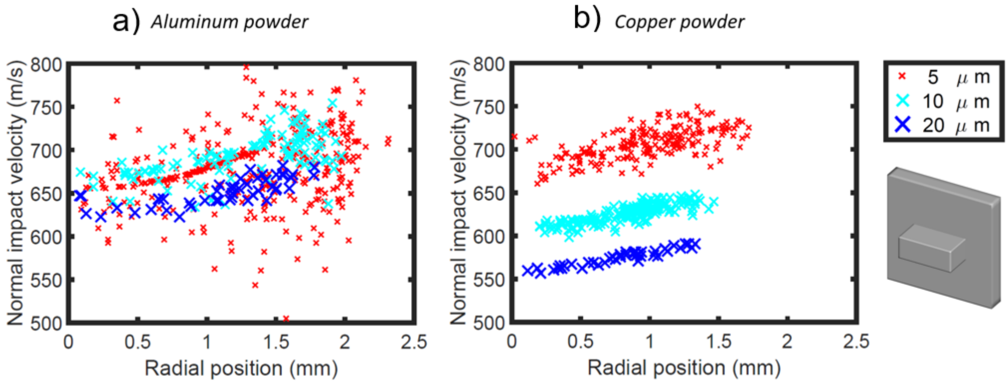

Figure 10. Normal impact velocities and radial location of (**a**) aluminum and (**b**) copper particles for the case with the vertical wall.

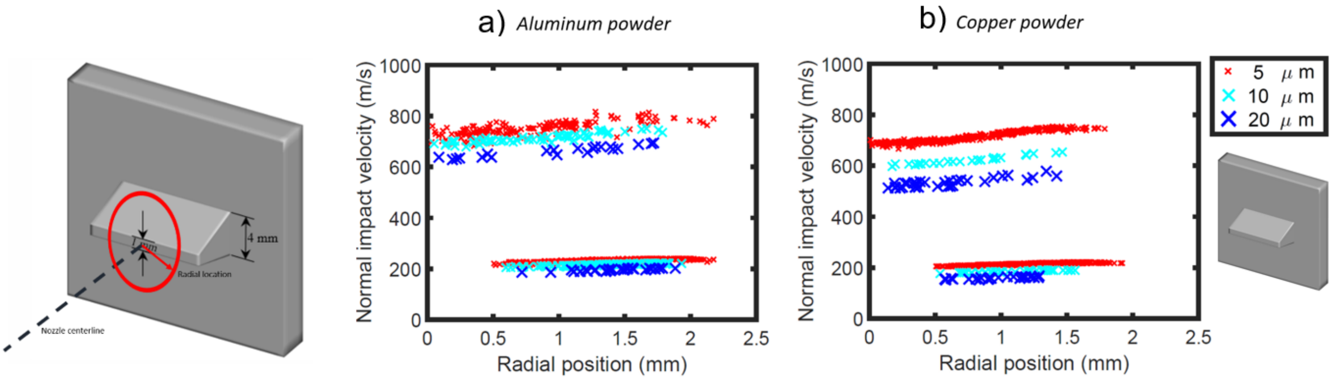

Figure 11. Normal impact velocities and radial location of (**a**) aluminum and (**b**) copper particles for the case with the inclined wall. The left image is prepared to show that the flow is not axisymmetric and the particles impact on both top and inclined planes.

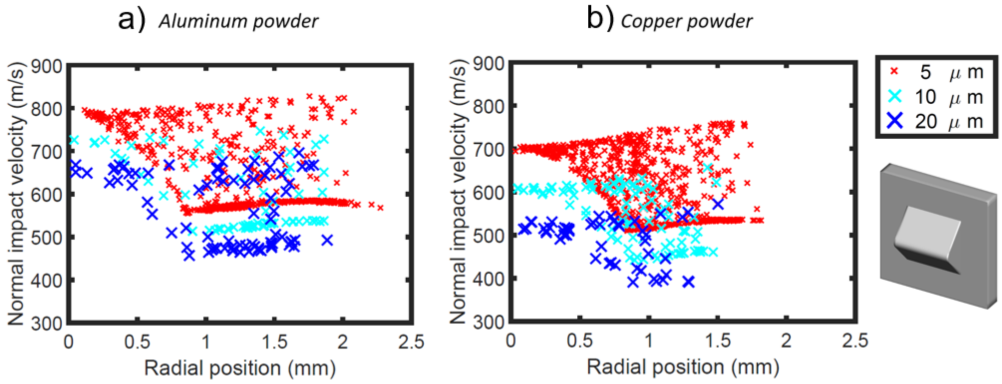

Figure 12. Normal impact velocities and radial location of (**a**) aluminum and (**b**) copper particles for the case with the smooth wall.

4. Conclusions

This study was focused on the gas flow and particle behavior adjacent to the substrate and walls. The effects of particle size and type as well as the shape of buildup layers in CSAM on the resolution of spraying and particles' trajectories were studied. A vertical wall (with uniform cross-section), an inclined wall (with non-uniform cross-section), and a smooth wall (based on the deposit profile observed in [25]) were investigated. For investigating the particle material, aluminum and copper powders were injected. It was found that the deviation of particles from the centerline is a function of shock diamonds, strength and location of bow shocks, and shapes of the objects placed on the substrate. Moreover, aluminum powders are found to be more affected by the object shape due to their lower density in comparison to copper. Different geometries of the walls provided different angles of impact which had a notable effect on the particle normal impact velocity. Particle deviation due to the presence of strong bow shock reduces the resolution of deposition. It also explains that to manufacture objects with small features, in addition to optimizing the operating conditions, modification of the nozzle geometry such as exit diameter, diverging part length, and nozzle shape should be taken into the account. This finding triggers a motivation for exploring other operating conditions and new designs for nozzles in future works.

Author Contributions: Conceptualization, S.G. and M.J.; methodology, S.G. and M.J.; software, S.G.; writing—original draft preparation, S.G.; writing—review and editing, M.J. All authors have read and agreed to the published version of the manuscript.

Funding: This research received no external funding.

Institutional Review Board Statement: Not applicable.

Informed Consent Statement: Not applicable.

Data Availability Statement: Not applicable.

Acknowledgments: The authors would like to thank Calcul Quebec (www.calculquebec.ca, accessed on 12 October 2022) and Digital Research Alliance of Canada (https://alliancecan.ca/en, accessed on 12 October 2022) for providing the computing resources.

Conflicts of Interest: The authors declare no conflict of interest.

References

1. Guo, D.; Kazasidis, M.; Hawkins, A.; Fan, N.; Leclerc, Z.; MacDonald, D.; Nastic, A.; Nikbakht, R.; Ortiz-Fernandez, R.; Rahmati, S.; et al. Cold Spray: Over 30 Years of Development toward a Hot Future. *J. Therm. Spray Technol.* **2022**, *31*, 866–907. [CrossRef]
2. Chen, C.; Xie, Y.; Yan, X.; Yin, S.; Fukanuma, H.; Huang, R.; Zhao, R.; Wang, J.; Ren, Z.; Liu, M.; et al. Effect of hot isostatic pressing (HIP) on microstructure and mechanical properties of Ti6Al4V alloy fabricated by cold spray additive manufacturing. *Addit. Manuf.* **2019**, *27*, 595–605. [CrossRef]

3. Yin, S.; Cavaliere, P.; Aldwell, B.; Jenkins, R.; Liao, H.; Li, W.; Lupoi, R. Cold spray additive manufacturing and repair: Fundamentals and applications. *Addit. Manuf.* **2018**, *21*, 628–650. [CrossRef]
4. Schmidt, T.; Assadi, H.; Gärtner, F.; Richter, H.; Stoltenhoff, T.; Kreye, H.; Klassen, T. From particle acceleration to impact and bonding in cold spraying. *J. Therm. Spray Technol.* **2009**, *18*, 794. [CrossRef]
5. Luo, X.-T.; Yao, M.-L.; Ma, N.; Takahashi, M.; Li, C.-J. Deposition behavior, microstructure and mechanical properties of an in-situ micro-forging assisted cold spray enabled additively manufactured Inconel 718 alloy. *Mater. Des.* **2018**, *155*, 384–395. [CrossRef]
6. Kosarev, V.F.; Klinkov, S.V.; Melamed, B.M.; Nepochatov, Y.K.; Ryashin, N.S.; Shikalov, V.S. Cold spraying for power electronics: Deposition of thick topologically patterned copper layers on ceramics. *AIP Conf. Proc.* **2018**, *2027*, 030047.
7. Shikalov, V.S.; Klinkov, S.V.; Kosarev, V.F. Cold spray deposition of aluminum coating onto an erodible material. *Thermophys. Aeromech.* **2019**, *26*, 729–737. [CrossRef]
8. Sova, A.; Smurov, I.; Doubenskaia, M.; Petrovskiy, P. Deposition of aluminum powder by cold spray micronozzle. *Int. J. Adv. Manuf. Technol.* **2018**, *95*, 3745–3752. [CrossRef]
9. Sova, A.; Grigoriev, S.; Okunkova, A.; Smurov, I. Potential of cold gas dynamic spray as additive manufacturing technology. *Int. J. Adv. Manuf. Technol.* **2013**, *69*, 2269–2278. [CrossRef]
10. Assadi, H.; Kreye, H.; Gärtner, F.; Klassen, T. Cold spraying—A materials perspective. *Acta Mater.* **2016**, *116*, 382–407. [CrossRef]
11. Bagherifard, S.; Monti, S.; Zuccoli, M.V.; Riccio, M.; Kondás, J.; Guagliano, M. Cold spray deposition for additive manufacturing of freeform structural components compared to selective laser melting. *Mater. Sci. Eng. A* **2018**, *721*, 339–350. [CrossRef]
12. Oyinbo, S.T.; Jen, T.-C. Investigation of the process parameters and restitution coefficient of ductile materials during cold gas dynamic spray (CGDS) using finite element analysis. *Addit. Manuf.* **2020**, *31*, 100986. [CrossRef]
13. Garmeh, S.; Jadidi, M.; Dolatabadi, A. Three-dimensional modeling of cold spray for additive manufacturing. *J. Therm. Spray Technol.* **2020**, *29*, 38–50. [CrossRef]
14. Samareh, B.; Dolatabadi, A. Dense particulate flow in a cold gas dynamic spray system. *J. Fluids Eng.* **2008**, *130*, 81702. [CrossRef]
15. Jenkins, R.; Aldwell, B.; Yin, S.; Chandra, S.; Morgan, G.; Lupoi, R. Solid state additive manufacture of highly-reflective Al coatings using cold spray. *Opt. Laser Technol.* **2019**, *115*, 251–256. [CrossRef]
16. Cavaliere, P.; Silvello, A. Processing parameters affecting cold spay coatings performances. *Int. J. Adv. Manuf. Technol.* **2014**, *71*, 263–277. [CrossRef]
17. Sova, A.; Okunkova, A.; Grigoriev, S.; Smurov, I. Velocity of the particles accelerated by a cold spray micronozzle: Experimental measurements and numerical simulation. *J. Therm. Spray Technol.* **2013**, *22*, 75–80. [CrossRef]
18. Wu, H.; Xie, X.; Liu, M.; Verdy, C.; Zhang, Y.; Liao, H.; Deng, S. Stable layer-building strategy to enhance cold-spray-based additive manufacturing. *Addit. Manuf.* **2020**, *35*, 101356. [CrossRef]
19. Wu, H.; Liu, S.; Zhang, Y.; Liao, H.; Raoelison, R.-N.; Deng, S. New process implementation to enhance cold spray-based additive manufacturing. *J. Therm. Spray Technol.* **2021**, *30*, 1284–1293. [CrossRef]
20. Ikeuchi, D.; Vargas-Uscategui, A.; Wu, X.; King, P.C. Data-efficient neural network for track profile modelling in cold spray additive manufacturing. *Appl. Sci.* **2021**, *11*, 1654. [CrossRef]
21. Vanerio, D.; Kondas, J.; Guagliano, M.; Bagherifard, S. 3D modelling of the deposit profile in cold spray additive manufacturing. *J. Manuf. Process.* **2021**, *67*, 521–534. [CrossRef]
22. Özdemir, O.Ç.; Conahan, J.M.; Müftü, S. Particle Velocimetry, CFD, and the Role of Particle Sphericity in Cold Spray. *Coatings* **2020**, *10*, 1254. [CrossRef]
23. Ozdemir, O.C.; Chen, Q.; Muftu, S.; Champagne, V.K. Modeling the continuous heat generation in the cold spray coating process. *J. Therm. Spray Technol.* **2019**, *28*, 108–123. [CrossRef]
24. Sudhan, K.H.; Prasad, G.K.; Kothurkar, N.K.; Srikrishnan, A.R. Studies on supersonic cold spray deposition of microparticles using a bell-type nozzle. *Surf. Coat. Technol.* **2020**, *383*, 125244. [CrossRef]
25. Kotoban, D.; Grigoriev, S.; Okunkova, A.; Sova, A. Influence of a shape of single track on deposition efficiency of 316L stainless steel powder in cold spray. *Surf. Coat. Technol.* **2017**, *309*, 951–958. [CrossRef]
26. Samareh, B.; Stier, O.; Lüthen, V.; Dolatabadi, A. Assessment of CFD modeling via flow visualization in cold spray process. *J. Therm. Spray Technol.* **2009**, *18*, 934. [CrossRef]
27. Samareh, B.; Dolatabadi, A. A three-dimensional analysis of the cold spray process: The effects of substrate location and shape. *J. Therm. Spray Technol.* **2007**, *16*, 634–642. [CrossRef]
28. Fluent, A. *Ansys Fluent Theory Guide*; ANSYS Inc.: Canonsburg, PA, USA, 2013.
29. Jadidi, M.; Moghtadernejad, S.; Dolatabadi, A. Numerical modeling of suspension HVOF spray. *J. Therm. Spray Technol.* **2016**, *25*, 451–464. [CrossRef]
30. Jadidi, M.; Yeganeh, A.Z.; Dolatabadi, A. Numerical study of suspension HVOF spray and particle behavior near flat and cylindrical substrates. *J. Therm. Spray Technol.* **2018**, *27*, 59–72. [CrossRef]
31. Jadidi, M.; Moghtadernejad, S.; Dolatabadi, A. A comprehensive review on fluid dynamics and transport of suspension/liquid droplets and particles in High-Velocity Oxygen-Fuel (HVOF) thermal spray. *Coatings* **2015**, *5*, 576–645. [CrossRef]
32. Faeth, G.M. Spray Atomization and Combustion. In Proceedings of the 24th Aerospace Sciences Meeting, Reno, NV, USA, 6–9 January 1986. [CrossRef]
33. Amsden, A.A.; O'Rourke, P.J.; Butler, T.D. *KIVA-II: A Computer Program for Chemically Reactive Flows with Sprays*; Technical Report LA-11560-MS, UC-96; Los Alamos National Lab: Los Alamos, NM, USA, 1989.

34. Crowe, C.T. Drag coefficient of particles in a rocket nozzle. *AIAA J.* **1967**, *5*, 1021–1022. [CrossRef]
35. Champagne, V.K.; Helfritch, D.J.; Dinavahi, S.P.G.; Leyman, P.F. Theoretical and experimental particle velocity in cold spray. *J. Therm. Spray Technol.* **2011**, *20*, 425–431. [CrossRef]
36. Jen, T.-C.; Li, L.; Cui, W.; Chen, Q.; Zhang, X. Numerical investigations on cold gas dynamic spray process with nano- and microsize particles. *Int. J. Heat Mass Transf.* **2005**, *48*, 4384–4396. [CrossRef]
37. Lupoi, R.; O'Neill, W. Powder stream characteristics in cold spray nozzles. *Surf. Coat. Technol.* **2011**, *206*, 1069–1076. [CrossRef]
38. Zabihi Yeganeh, A.; Jadidi, M.; Moreau, C.; Dolatabadi, A. Numerical modeling of aerosol deposition process. *Surf. Coat. Technol.* **2019**, *370*, 269–287. [CrossRef]
39. Schmidt, K.; Buhl, S.; Davoudi, N.; Godard, C.; Merz, R.; Raid, I.; Kerscher, E.; Kopnarski, M.; Müller-Renno, C.; Ripperger, S.; et al. Ti surface modification by cold spraying with TiO_2 microparticles. *Surf. Coat. Technol.* **2017**, *309*, 749–758. [CrossRef]
40. Gilmore, D.L.; Dykhuizen, R.C.; Neiser, R.A.; Smith, M.F.; Roemer, T.J. Particle velocity and deposition efficiency in the cold spray process. *J. Therm. Spray Technol.* **1999**, *8*, 576–582. [CrossRef]
41. Zhu, W.; Zhang, X.; Zhang, M.; Tian, X.; Li, D. Integral numerical modeling of the deposition profile of a cold spraying process as an additive manufacturing. *Prog. Addit. Manuf.* **2019**, *4*, 357–370. [CrossRef]
42. Ikeuchi, D.; Vargas-Uscategui, A.; Wu, X.; King, P.C. Neural network modelling of track profile in cold spray additive manufacturing. *Materials* **2019**, *12*, 2827. [CrossRef]
43. Cao, C.; Li, W.; Zhang, Z.; Yang, X.; Xu, Y. Cold Spray Additive Manufacturing of Ti6Al4V: Special Nozzle Design Using Numerical Simulation and Experimental Validation. *Coatings* **2022**, *12*, 210. [CrossRef]